Ordering in rolled-up single-walled ferromagnetic nanomembranes

Andrzej Janutka[a]

[a]*Department of Theoretical Physics, Faculty of Fundamental Problems of Technology, Wroclaw University of Technology, 50-370 Wrocław, Poland*

arXiv:1603.04883v2 [cond-mat.mes-hall] 9 Sep 2016

Abstract

Magnetization of soft-ferromagnetic nano- and microtubes of nanometer-thin walls (a single-widening rolled-up nanomembranes) is theoretically studied using analytical and numerical approaches including different stress-induced anisotropies. Within the analytical study, we consider magnetostatic effects qualitatively, with an effective anisotropy, while they are fully treated in the micromagnetic simulations (limited to the tubes of submicrometer diameters however). Basic types of the periodic ordering have been established and their presence in nanotubes of polycrystalline Permalloy and cobalt has been verified within the simulations. The domain structure is basically determined by a material-deposition-induced helical stress or a cooling-induced axial stress via the volume magnetostriction while it is influenced by the distribution of magnetic charges as well. Also, it is dependent on the initial state of the magnetization process.

Keywords: ferromagnetic nanotube, ferromagnetic microtube, stress-driven anisotropy, magnetic domain structure, analytical micromagnetism, micromagnetic simulations

[1]E-mail address: Andrzej.Janutka@pwr.edu.pl

1. Introduction

Ordering in a small ferromagnetic tube with very thin wall compared to its radius is difficult to anticipate since that structure shares features of the thin film and magnetic wire relevant to the magnetostatics (a radial anisotropy of the hard-axis type and easy long axis of the tube) with a strong stress-driven anisotropy dependent on fabrication conditions. Because of complexity of the anisotropy, there are many metastable states of the magnetization, thus, the ordering is sensitive to initial conditions and external factors. On the other hand, the tube is a very important geometry among magnetic nano- and micro-systems since tubular coverings enable modifications of magneto-transport; GMI effect, and magneto-optical properties of wires and fibers to be utilized for sensing applications [1, 2, 3]. Also, magnetic microtube can serve as a sensing pipe for magnetic nanofluids [4].

Techniques of manufacturing single-crystalline and polycrystalline micro- and nanotubes of magnetic materials include electrochemical and chemical routes [2, 5, 6, 7]. Highly efficient production methods are developed for magnetic microtubes of a thin wall. They are produced with sputtering in the form of microwire or microfiber coverings or rolled-up membranes of nanometer thicknesses [8, 9]. Note that an outer shell of the amorphous glass-coated magnetic microwire can be considered as a tube as well, albeit it strongly interacts with the inner core of the wire, (the glass-coated magnetic microwire is a single-phase system with a core-shell type magnetic ordering [10]), and its wall is quite thick relative to the wire radius [11, 12]. However, upon glass removal, the outer shell becomes very thin while the thickness of a domain wall (DW) that separates it from the inner core increases [13, 14]. This is accompanied by a reorganization of the domain structure and influences the GMI characteristics [15]. With regard to functionalized wires and fibers, there is a need for modeling the dynamics of the thin-wall tube magnetization. The first step to do in order to formulate an effective model is to understand dominant mechanisms responsible for ordering in the nano- and micro-tubes without external influences.

In microtubes of very small wall-thickness to radius ratio, the longitudinal easy-axis anisotropy of the magnetostatic origin is weaker than in tubes of a thick wall or in wires. Thus, influenced by the stress-driven anisotropy, the domain magnetization can strongly deviate from the long-axis direction even in very elongated systems. Moreover, the magnetostatically-induced hard-axis anisotropy (the hard axis is normal to the tube surface) is strong, which facilitates in-the-wall ordering (excluding singularities; vortex and antivortex cores) independent of the stress direction and sign of the volume magnetostriction. Despite the shape anisotropy is not well defined in the system with an inhomogeneous magnetization, any efficient analytical approach to establishing equilibrium states of the tube requires introducing such an effective anisotropy into the model. Full micromagnetic simulations are necessary to verify the validity of such a simplification to the nanotubes while they are not any efficient alternative to the analytical evaluations of the microtube characteristics at present. It is because, simulating microtubes requires too large computational resources.

The purpose of the present study is to identify basic equilibrium states of thin-wall microtubes and nanotubes including longitudinal, transverse, and helical anisotropies. We compare static analytical and numerical solutions to the Landau-Lifshitz-Gilbert equation for nanotubes, modeling the magnetostatics effect with an effective anisotropy or performing full micromagnetic calculations, respectively. The evaluations are focused on the polycrystalline tubes of the most popular magnetic materials; Co and Py tubes. When exclude the crystalline anisotropy effect, important differences in ordering of these two materials follow from different saturation magnetizations. The influence of other factors (origin of the internal stress, initial state of the magnetization) on the formation of the magnetic texture is discussed as well.

In section II, a model of the thin-wall nano- and microtube is formulated, its analytical solutions are pointed out. Section III is devoted to presenting results of micromagnetic simulations of the process of tube ordering. Conclusions are collected in section IV.

2. Model

In our analytical approach to study the magnetization of a polycrystalline or amorphous tube, the LLG equation in 3D is included in the form

$$\begin{aligned} -\frac{\partial \mathbf{m}}{\partial t} &= \frac{J}{M_s}\mathbf{m}\times\Delta\mathbf{m} + \frac{\beta_1}{M_s}(\mathbf{m}\cdot\hat{i})\mathbf{m}\times\hat{i} \\ &-\frac{\beta_2}{M_s}\frac{[\mathbf{m}\cdot(0,y,z)]\mathbf{m}\times(0,y,z)}{(y^2+z^2)} \\ &+\frac{\beta_3}{M_s}\frac{[\mathbf{m}\cdot(0,-z,y)]\mathbf{m}\times(0,-z,y)}{(y^2+z^2)} \\ &+\frac{\beta_4}{M_s}(\mathbf{m}\cdot\mathbf{a})\mathbf{m}\times\mathbf{a} - \frac{\alpha}{M_s}\mathbf{m}\times\frac{\partial\mathbf{m}}{\partial t}. \quad (1) \end{aligned}$$

Here, $\hat{i}\equiv[1,0,0]$, (the wire is directed along the x axis), $M_s=|\mathbf{m}|$ represents the saturation magnetization, J denotes the exchange constant, ($J\equiv 2\gamma A_{ex}/M_s$; A_{ex} is called an exchange stiffness while γ a gyromagnetic factor), β_1, β_2, and β_3 determine the strength of effective axial, radial, and circumferential anisotropies, respectively. An additional anisotropy in the tube wall is included with the β_4 constant. In the relevant term of the torque, $\mathbf{a}$ is a combination of $\hat{i}$ and $(0,-z,y)/\sqrt{y^2+z^2}$ vectors and $|\mathbf{a}|=1$.

In order to establish main contributions to the anisotropy constants, utilizing analogies to the tubes, we adapt elements of the theory of elasticity of the amorphous and polycrystalline glass-coated microwires which is well developed [10]. According to this theory, the internal stress can be created at two production stages; the solidification of the magnetic material and its cooling that is a much slower process. The solidification of the magnetic microwire develops in the radial direction. In the surface layer of the microwire that can be considered as a tube, it produces equal to each other axial and circumferential components of the stress while the relevant radial stress is negligibly small. This kind of stress follows from a homogeneous shrinking of the inside surface of the tube compared to the outside surface and we call it a "solidification stress", (in the body of the "rapidly-solidified" wire, the relevant stress is created layer by layer). In the presence of that stress, in the tubes made of amorphous or polycrystalline materials, the magnetostriction that is of the volume type only (isotropic) is expected to equally contribute to the β_1 and β_3 constants of the anisotropy.

However, the tube manufacturing is a different process from the wire production in general. Typically, the magnetic tubes are formed via rolling-up planar magnetic (created with sputtering or evaporation) layers or via direct sputtering on a surface of cylindrical wires. Those methods of the material deposition are accompanied by another "solidification stress" and a resulting easy direction in the magnetic layer that is parallel or perpendicular to the sputtering (evaporation) plane usually. While the rapid-solidification stress is not expected to be strong in a very thin film, the directed sputtering can result in the creation of a significant anisotropy relevant to β_4 constant [16, 17]. Note that such an anisotropy can be weakened or completely removed via annealing. That "helical" anisotropy in a magnetic tube has been modeled previously in [18].

Another type of the stress can dominate in multi-layered tubes. Since the thermal expansion is isotropic within the cross-section of the double-layer tube, for a sufficiently long tube, a difference in the thermal expansion coefficients of the magnetic and non-magnetic layers results in equal to each other radial and circumferential stresses as well as in a much higher axial stress which are induced during the slow cooling process. Therefore, in the amorphous or polycrystalline tubes, the "cooling stress" contributions to the constants of the radial and circumferential anisotropies are equal.

Denoting the magnetostatic, solidification, and cooling contributions to the anisotropy constants with the relevant indices; $\beta_i=\beta_i^{(ms)}+\beta_i^{(solid)}+\beta_i^{(cool)}$, $(i=1,2,3)$, we establish $\beta_2^{(cool)}=-\beta_3^{(cool)}$, $\beta_2^{(solid)}\approx 0$, $\beta_1^{(solid)}=\beta_3^{(solid)}$, $\beta_2^{(ms)}>0$, $\beta_1^{(ms)}\geq\beta_3^{(ms)}\approx 0$. In particular, it follows from above formulae that the effective cooling-induced anisotropy is uniaxial with the anisotropy axis oriented along the tube. In the limit of infinitely thin tube, the axial contribution to the shape anisotropy becomes negligible; $\beta_2^{(ms)}\gg\beta_1^{(ms)}\approx 0$.

Searching for the static solutions to (1) and performing the micromagnetic simulations of tubes, we restrict our considerations to the regimes of solidification-dominated stress and cooling-dominated stress. Also, we focus on thin-wall tubes taking $\beta_1^{(ms)}=\beta_3^{(ms)}=0$ in analytical evaluations. Thus, we consider a quasi-2D system with a periodic boundary condition relevant to the tube geometry. It is basically in-the-plane magnetized due to the magnetostatics.

2.1. Tubes with cooling-dominated stress

According to the above analysis of the anisotropy constants, the cooling-dominated stress produces an axial anisotropy mainly. Therefore, having in mind the aim of obtaining the periodic along the tube axis solutions, first, we seek for single-DW solutions assuming the domains to be magnetized longitudinally to the wire. Thus, the boundary condition $\lim_{|x|\to\infty}\mathbf{m} = \pm(M_s, 0, 0)$ is satisfied. Using a systematic approach of the soliton theory, we look for the equations of motion in the multi-linear form. Following [19], we apply the transform

$$m_+ = \frac{2M_s}{f^*/g + g^*/f}, \qquad m_x = M_s\frac{f^*/g - g^*/f}{f^*/g + g^*/f}, \quad (2)$$

where $m_\pm \equiv m_y \pm \mathrm{i}m_z$, and we find tri-linear equations of motion for the complex functions $g(x,y,z,t)$, $f(x,y,z,t)$ (secondary dynamical variables)

$$\begin{aligned} -f\mathrm{i}D_t f^*\cdot g = f\left[\alpha D_t + J(D_x^2+D_y^2+D_z^2)\right]f^*\cdot g \\ +Jg^*(D_x^2+D_y^2+D_z^2)g\cdot g \\ -\frac{2\beta_1+\beta_2-\beta_3}{2}|f|^2 g - \frac{\beta_2+\beta_3}{2}\frac{(y+\mathrm{i}z)^2}{y^2+z^2}f^{*2}g^* \\ -g^*\mathrm{i}D_t f^*\cdot g = g^*\left[\alpha D_t - J(D_x^2+D_y^2+D_z^2)\right]f^*\cdot g \\ -Jf(D_x^2+D_y^2+D_z^2)f^*\cdot f^* \\ +\frac{2\beta_1+\beta_2-\beta_3}{2}|g|^2 f^* + \frac{\beta_2+\beta_3}{2}\frac{(y-\mathrm{i}z)^2}{y^2+z^2}g^2 f. \end{aligned} \quad (3)$$

Here D_t, D_x, D_y, D_z denote Hirota operators of differentiation $D_x^n b(x,y,z,t)\cdot c(x,y,z,t) \equiv (\partial/\partial x - \partial/\partial x')^n \times$ $\times\, b(x,y,z,t)c(x',y',z',t')|_{x=x',y=y',z=z',t=t'}$.

Specific stationary solutions of the single-DW type (for $\beta_4 = 0$) have been identified applying the ansatz

$$f = 1, \qquad g = \mathrm{e}^{kx+\mathrm{i}\phi+qR\cdot\arctan(z/y)} \quad (4)$$

to the limit of thin-wall tube $\sqrt{y^2+z^2} = R$. In the case $\beta_2+\beta_3 = 0$, denoting $q' \equiv \mathrm{Re}q$, $q'' \equiv \mathrm{Im}q$, one finds

$$k'k'' = -q'q'', \;\; k'^2 - k''^2 + q'^2 - q''^2 = \frac{K_a}{A_{ex}}, \quad (5)$$

where $K_a \equiv M_s[\beta_1 + (\beta_2-\beta_3)/2]/2\gamma$. This case corresponds to the uniaxial effective anisotropy whose axis is oriented along the tube, while the DW solutions are similar to ones studied in the context of relatively-thick (submicrometer) ferromagnetic layers [20, 21]. In our effective description of the thin-wall tube, via assuming the domain magnetization to be oriented in the tube surface, the magnetostatic contributions to the anisotropy coefficient β_2^{ms} are removed, thus, $\beta_i^{ms} = 0$ for $i = 1,2,3$. Hence, with the condition $\beta_2+\beta_3 = 0$, we consider the anisotropy due to the cooling-dominated stress in the tube. The conditions of periodicity $q' = 0$, $q'' = l/R$ must be included, where l is integer. The explicit form of the magnetization distribution (written in the cylindrical coordinates; $[x,\rho,\varphi] \equiv [x, \sqrt{y^2+z^2}, \arctan(z/y)]$) is given by

$$\begin{aligned} m_+(x,\varphi) &= M_s\mathrm{e}^{\mathrm{i}(\phi+q''R\varphi+k''x)}\mathrm{sech}\left(k'x+q'R\varphi\right), \\ m_x(x,\varphi) &= -M_s\tanh\left(k'x+q'R\varphi\right). \end{aligned} \quad (6)$$

Having found the above single-DW solutions, we modify them when looking for the patterned (multi-domain) periodic textures. We find novel magnetization structures just via changing specific hyperbolic functions $\mathrm{sech}(u)$, $\tanh(u)$ in (6) into the Jacobi elliptic functions; $\mathrm{cn}(u,s^2)$, $\mathrm{sn}(u,s^2)$, $s^2 \in [0,1)$. This often utilized method of finding periodic solutions from soliton solutions is based on common properties of the corresponding pairs of the hyperbolic and elliptic Jacobi functions. In particular, describing static DWs with the LLG equation, similarity of the relation $\mathrm{sech}(u)\mathrm{d}^2\tanh(u)/\mathrm{d}u^2 - \tanh(u)\mathrm{d}^2\mathrm{sech}(u)/\mathrm{d}u^2$ $= -\mathrm{sech}(u)\tanh(u)$ to $\mathrm{cn}(u,s^2)\mathrm{d}^2\mathrm{sn}(u,s^2)/\mathrm{d}u^2$ $-\,\mathrm{sn}(u,s^2)\mathrm{d}^2\mathrm{cn}(u,s^2)/\mathrm{d}u^2 = -s^2\mathrm{cn}(u,s^2)\mathrm{sn}(u,s^2)$ allows for an easy verification of the validity of our method. Inserting this way modified magnetization field into (1), one finds the parameters of the periodic solutions to must satisfy similar conditions to (5). Two of the basic types of such solutions are distinguished by the orientation of the DWs parallel to the domain magnetization. Such an orientation of the DW relative to the domains is preferred by the condition of compensation of the positive and negative magnetic volume charges $-\nabla\cdot\mathbf{m}$, [17].

The first one of the distinguished periodic solutions is

$$\begin{aligned} m_+(x,\varphi) &= M_s\mathrm{e}^{\mathrm{i}(\phi+q''R\varphi)}\mathrm{sn}\left(k'x/s, s^2\right) \\ m_x(x,\varphi) &= -M_s\mathrm{cn}\left(k'x/s, s^2\right), \end{aligned} \quad (7)$$

with $k'^2 + q''^2 = -K_a/A_{ex}$, and $q''R$ to be an integer. In the case of $\phi = \pi/2, 3\pi/2$, and $s^2 \approx 1$, (7) relates to the long axis of the tube to be magnetically hard.

Another static solution to (1) is approximately described with

$$\begin{aligned} m_+(x,\varphi) &= M_s\mathrm{e}^{\mathrm{i}\phi}\left[\mathrm{cn}\left(\tilde{k}''x/w, w^2\right)\right. \\ &\quad \left.+\mathrm{isn}\left(\tilde{k}''x/w, w^2\right)\right]\mathrm{cn}\left(q'R\varphi/s, s^2\right) \\ m_x(x,\varphi) &= -M_s\mathrm{sn}\left(q'R\varphi/s, s^2\right), \end{aligned} \quad (8)$$

where $q'^2 - \tilde{k}''^2 = M_s^2K_a/2A_{ex}$. For the single walled tube, $q'2\pi R/s$ is equal to a multiple of the period of the Jacobi functions which is the elliptic integral $K(s) = \int_0^{2\pi}[1 - s^2\sin^2(\theta)]^{-1/2}\mathrm{d}\theta$, ($q'2\pi R/s = nK(s)$, where n is integer). In the case $w \neq 0$, (8) satisfies (1) on the lines $q'R\varphi/s = K(s)h$, where $h = 0, 1, \ldots, n-1$, and on the lines $\tilde{k}''x/w = K(w)m$, where $m = 0, \pm1, \pm2, \ldots$. Thus, (1) is satisfied on lines of a net that covers the tube surface. Therefore, we consider (8) to be an approximate representation of a possible texture. The intersections of the lines of both series (the net sites) coincide with the centers of vortices or antivortices inherent in the texture.

In the $w = 0$ limit case of (8), that is reached via exchanging $\tilde{k}^{''}/w$ into $k^{''}$, thus, exchanging $\mathrm{cn}(\tilde{k}^{''}x/w, w^2) + \mathrm{isn}(\tilde{k}^{''}x/w, w^2)$ in the first of equations (8) into $\mathrm{e}^{\mathrm{i}k^{''}x}$, one obtains a strict solution to (1). Its parameters satisfy $q^{'2} - k^{''2} = K_a/A_{ex}$.

2.2. Tubes with solidification-dominated stress

According to previous section considerations, in the thin-wall tube, the solidification contribution to the constant of the circumferential anisotropy is equal to that of the axial anisotropy; $\beta_1^{(solid)} = \beta_3^{(solid)}$, and the contribution to the radial anisotropy constant $\beta_2^{(solid)}$ is equal to zero. However, such a two-axis anisotropy is equivalent to the radial anisotropy whose type (easy-axis or hard-axis) is determined by the sign of the magnetostriction constant. Thus, the consequence of the solidification stress is the enhancement or attenuation of the magnetostatically-induced radial anisotropy of the hard-axis type. Provided the summary radial hard-axis anisotropy is sufficiently strong, the efficient way to describe the magnetic ordering is applying the XY model on the curved surface (the tube surface) spanned on the axial (X) and circumferential (Y) directions. Detailed justification of that approach to the ordering in thin soft-ferromagnetic film has been given elsewhere [22]. We write the magnetization in the cylindrical coordinates and assume $m_\rho = 0$ and $m_x + \mathrm{i}m_\varphi = M_s\mathrm{e}^{\mathrm{i}(\eta+\theta)}$ with $\eta = \mathrm{const}$. Insertion of the above magnetization into (1), in the static case, leads to the Laplace equation

$$\frac{\partial^2\theta}{\partial x^2} + \frac{1}{R^2}\frac{\partial^2\theta}{\partial\varphi^2} = 0. \tag{9}$$

Utilizing its DW solution from [22], one arrives at

$$\begin{aligned} m_x &= M_s\frac{\cos(\eta)b - \sin(\eta)a}{\sqrt{a^2+b^2}}, \\ m_\varphi &= M_s\frac{\sin(\eta)b + \cos(\eta)a}{\sqrt{a^2+b^2}}, \end{aligned} \tag{10}$$

where $a \equiv \sin(k^{''}x + q^{''}R\varphi)$, $b \equiv \sinh(k^{'}x + q^{'}R\varphi)$, and the conditions $k^{'2} - k^{''2} + q^{'2} - q^{''2} = 0$, $k^{'}k^{''} = -q^{'}q^{''}$ are satisfied. This single-DW solution cannot satisfy the periodic boundary condition, $\mathbf{m}(x,\varphi) \neq \mathbf{m}(x,\varphi + 2\pi)$ for $q^{'} \neq 0$. Therefore, it is not relevant to the single-walled tube. Exchanging $b \equiv \sinh(k^{'}x + q^{'}R\varphi)$ in (10) into $b \equiv \mathrm{sn}(k^{'}x/s + q^{'}R\varphi/s, s^2)/\mathrm{dn}(k^{'}x/s + q^{'}R\varphi/s, s^2)$, for $|s|$ very close to 1, one obtains an approximate solution to the XY model that is periodic in the axial direction and in the circumferential direction provided $q^{''}R = l$ and $q^{'}2\pi R \approx nK(s)$. Here, n and l are integers. That solution represents a system of many parallel DWs. When $\tan(\eta) = q^{'}/k^{'}$, the DWs are parallel to the magnetization of the domains.

The direction of the DW relative to the tube axes follows from a competition between axial (shape) anisotropy of the tube and the anisotropy due to the direction of the material deposition. Therefore, it is dependent of the length of the tube. We include both anisotropies into the reduced (XY) model just via the boundary condition on the direction of the domain magnetization, the angle η, similar to the description of DWs in soft-magnetic nanostripes [22, 23]. However, unlike in the nanostripes whose edges strongly affect the DW texture (via stabilizing singularities; antivortices), in the case of the infinite planar layers or tube walls, the (anti)vortex containing DWs are not preferable for sufficiently thin systems while Neel DWs are [20, 24]. Those DWs are not described with the XY model.

Besides the geometry of the tube (thickness of its wall), the applicability of the XY model is dependent on the ratio of the magnetostatic exchange length $l_{ms} \equiv \sqrt{2A_{ex}/\mu_0 M_s^2}$ to the exchange length of the solidification-stress-induced (helical) anisotropy $l_K \equiv \sqrt{A_{ex}/K_h^{(solid)}}$, where $K_h^{(solid)} \equiv M_s\beta_4^{(solid)}/2\gamma$. The magnetostatic field and the helical-anisotropy field compete in the area of the DW. When, l_{ms} is significantly smaller than l_K, (the magnetostatic field is stronger than the helical-anisotropy field), which enforces the ordering to be completely confined to the tube surface, (the Neel-DWs are preferable instead of the cross-tie DWs). In the parameter range of l_{ms} close to l_K, both fields can cancel each other, which makes the XY model applicable. In the former case, ($l_{ms} \ll l_K$), the magnetostatic exchange length corresponds to DW width and the magnetostatic field in the DW area can be modeled with a $M_s\beta_4^{(ms)} \equiv 2\gamma K_h^{(ms)} \sim \gamma\mu_0 M_s^2$ contribution to the anisotropy constant in (1) while the DW magnetization can be described with direct solutions to the LLG equation.

For $\beta_2 + \beta_3 = 0$, in the limit of weak shape (axial) anisotropy; $|\beta_1| \ll \beta_4$, the relevant DW texture is described with a rotated in the $x - \varphi$ plane function (6);

$$\begin{aligned} m_x(x,\varphi) &= -M_s\cos(\eta)c - M_s\sin(\eta)d, \\ m_\rho(x,\varphi) &= M_s e, \\ m_\varphi(x,\varphi) &= -M_s\sin(\eta)c + M_s\cos(\eta)d, \end{aligned} \tag{11}$$

where

$$\begin{aligned} c &\equiv -\tanh(k^{'}x + q^{'}R\varphi), \\ d &\equiv [\cos(\varphi)\cos(\phi + q^{''}R\varphi + k^{''}x) + \sin(\varphi) \\ &\quad \times\sin(\phi + q^{''}R\varphi + k^{''}x)]\mathrm{sech}(k^{'}x + q^{'}R\varphi), \\ e &\equiv [-\sin(\varphi)\cos(\phi + q^{''}R\varphi + k^{''}x) + \cos(\varphi) \\ &\quad \times\sin(\phi + q^{''}R\varphi + k^{''}x)]\mathrm{sech}(k^{'}x + q^{'}R\varphi), \end{aligned} \tag{12}$$

and

$$k^{'}k^{''} = -q^{'}q^{''}, \tag{13}$$

$$k^{'2} - k^{''2} + q^{'2} - q^{''2} = \frac{K_h}{A_{ex}}. \tag{14}$$

Here, $K_h = K_h^{(ms)} + K_h^{(solid)}$, and $K_h^{(ms)}K_h^{(solid)} < 0$. We expect the DW to be parallel to the domain magnetization, thus; $\tan(\eta) = q^{'}/k^{'}$. Similar to the formula (10), the formula (12) is not applicable to single-walled tube

because one cannot implement the periodic boundary condition; $\mathbf{m}(x,\varphi) \neq \mathbf{m}(x,\varphi+2\pi)$. In order to do it, we find another solution to (1) via exchanging in (12) the hyperbolic functions into elliptic ones; $\mathrm{sech}(k^{'}x+q^{'}R\varphi) \rightarrow \mathrm{sn}(k^{'}x/s+q^{'}R\varphi/s, s^2)$ and $\tanh(k^{'}x+q^{'}R\varphi) \rightarrow \mathrm{cn}(k^{'}x/s+q^{'}R\varphi/s, s^2)$, as well as transforming the condition (14) into

$$k^{'2}+k^{''2}+q^{'2}+q^{''2}=-\frac{K_h}{A_{ex}}. \qquad (15)$$

While the formulae (11)-(14) are capable to describe cross-tie DWs even in the case $\beta_4 \neq 0$, with $|k^{'}| = |q^{'}|$ and $|q^{''}| = |k^{''}|$ for instance [21], the periodic boundary condition restricts values of $q^{'}$ and $q^{''}$ to discrete sets. Applied together with (13), (15), this condition drives $q^{''} = k^{''} = 0$. Therefore, those cross-tie DWs cannot be stabilized in the single-walled tube. Hence, unlike the DWs of the XY model, the present DW does not contain vortices nor antivortices, which provides basic distinction between the multi-domain textures relevant to different regimes of the description of the tubes with solidification-dominated stress.

3. Micromagnetic simulations

We have performed a series of micromagnetic simulations of the relaxation of thin-wall ferromagnetic tubes in order to verify the analytically obtained magnetization distributions. Simulating the tubes with the cooling-dominated stress, we apply the material parameters of cobalt. In [25], the cooling stress has been directly shown to can significantly overcome the solidification stress in the rolled-up Co nanomembrane, which results in qualitative changes in the hysteresis loops of the tubes with temperature. Dealing with the solidification-dominated stress, we include the parameters of Permalloy additionally, in order to examine systems of significantly different ratio of the magnetostatic exchange length l_{ms} to the exchange length of the stress-induced (helical) anisotropy l_K. Notice that the magnetostatic exchange lengths of Co and Py are the same ($l_{ms} = 5.2$nm) while their exchange stiffnesses A_{ex} are very different. The techniques of rolling-up the nanomembranes of these magnetic materials are well developed [25, 26], so as related nickel nanomembranes [9, 27, 28].

Due to the computational complexity, the diameters of the simulated structures are limited to submicrometer sizes. We applied OOMMF package [29]. The discretization size of the tube grid is 5nm in the YZ plane and 10nm in the X direction. The Gilbert damping constant is $\alpha = 0.5$.

3.1. Tubes with cooling-dominated stress

In the simulations of the Co tubes, the following material constants are used; the saturation magnetization $M_s = 1.4 \cdot 10^6$A/m, the exchange stiffness $A_{ex} = 3.3 \cdot 10^{-11}$J/m. Assuming the stress to be cooling-dominated, the stress-induced axial anisotropy of the easy-plane type is included

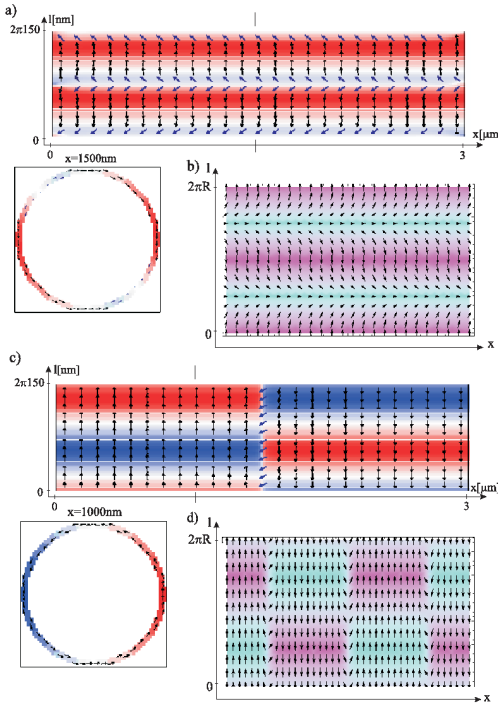

Figure 1: The textures established in the Co tube (of 300nm diameter, 3μm length, and 20nm wall thickness) with micromagnetic simulations, for the initial magnetization of the tube $[M_s/\sqrt{2}, M_s/\sqrt{2}, 0]$ (a), $[M_s, 0, 0]$ (c). For comparison to numerical results, analytical expressions for the tube magnetization are plotted; the texture relevant to the $w = 0$ limit of expression (8) and $k^{''} = 0$, $s \approx 0$, $|q^{'}|R \approx 1$ (b), and the texture relevant to (7) for $|s| = 1 - 6 \cdot 10^{-11}$, $|q^{''}|R = 1$ (d). In a) and c), the constant of (stress-induced) uniaxial anisotropy (of the [1,0,0] hard direction) is $K_a^{(cool)} = -1.5 \cdot 10^5$J/m^3. Here and below, $l \equiv R\varphi$ denotes the circumferential coordinate while area colors and their intensities indicate sign and value of m_y component of the magnetization. Arrow colors in the simulation-obtained plots indicate sign and value of m_x.

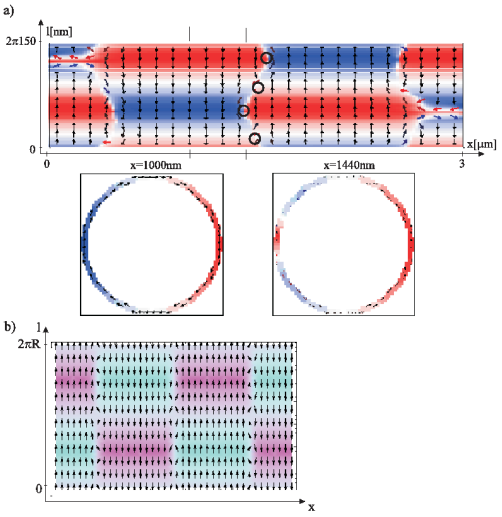

Figure 2: The texture established in the Co tube (of 300nm diameter, 3μm length, and 20nm wall thickness) with the initial magnetization of the tube $[0, M_s, 0]$ (a). Point singularities (vortices and antivortices) in the central DW are indicated by circles. For comparison to numerical results, analytical expression for the tube magnetization; the textures relevant to (7) for $|s| = 1 - 6 \cdot 10^{-11}$ and $|q^{''}|R = 4$ is plotted (b). The material parameters for a) are the same as in Fig. 1. The area (arrow) color and its intensity indicate sign and value of m_y (m_x) component of the magnetization, similar as in Fig. 1.

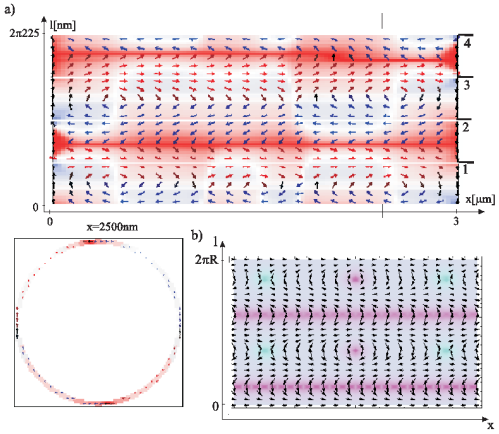

Figure 3: The texture established in the Co tube of 450nm diameter, 3μm length, and 20nm wall thickness with micromagnetic simulations, for the initial magnetization of the tube $[0, M_s, 0]$ (a). The constant of (stress-induced) uniaxial anisotropy (of the [1,0,0] hard direction) is $K_a^{(cool)} = -0.63 \cdot 10^5 \mathrm{J/m}^3$. Meaning of colors is the same as in Figs. 1-2. Four sections of the tube wall are indicated with numbers 1-4. For comparison to numerical results, relevant analytical expression for the tube magnetization is plotted (b). Sections $\pi R/2 < l < \pi R$ or $3\pi R/2 < l < 2\pi R$; [relevant to sections 1 and 3 of a)] are described with (8) for $q^{'2} \approx \tilde{k}^{''2}$, $|s| = 1 - 6 \cdot 10^{-3}$, $|w| = 1 - 6 \cdot 10^{-6}$, while others [relevant to sections 2 and 4 of a)] with the $w = 0$ limit of (8) and $k^{''} = 0$, $s \approx 0$, $|q^{'}|R \approx 2$.

with an anisotropy constant $K_a^{(cool)} \sim (-1)\cdot 10^4 \div (-1)\cdot 10^5 \mathrm{J/m^3}$, $[K_a^{(cool)} \sim M_s(\beta_1^{(cool)} - \beta_3^{(cool)})/2\gamma]$. In [25], a Co tube has been reported to possess the axial anisotropy relevant to $K_a \sim 10^3 \mathrm{J/m^3}$ for the diameter of several micrometers while cooling of the tube to result in decrease of the anisotropy constant to $K_a \sim (-1)\cdot 10^4 \mathrm{J/m^3}$, (thus, in the change of the easy-axis into the hard-axis). Decreasing the tube diameter down to several hundreds of nanometers, the absolute value of the density of energy of the stress-driven anisotropy is expected to increase. The Co tubes of 300nm diameter, 20nm wall thickness and 3μm length, and of the arbitrarily chosen anisotropy constant $K_a^{(cool)} = -1.5\cdot 10^5 \mathrm{J/m^3}$ have been simulated with different initial conditions. The calculations begun with the homogeneous magnetization $\mathbf{m}(t=0) = [M_s/\sqrt{2}, M_s/\sqrt{2}, 0]$ and finished with the stable configuration of Fig. 1a. Correspondingly, initialized with the longitudinal magnetization $\mathbf{m}(t=0) = [M_s, 0, 0]$ simulation ended with the texture of Fig. 1c, while the perpendicular magnetization $\mathbf{m}(t=0) = [0, M_s, 0]$ evolved to that of Fig. 2a. One sees that there are many stable (metastable) states of the tube magnetization which realize under specific initial conditions. They correspond to different stationary solutions to the LLG equation.

In particular; Fig. 1a corresponds to a field state (8) with $w=0$, $k^{''}=0$, $s^2 \approx 0$, $q^{'} 2\pi R/s = \pm K(s)$, $\phi = \pi/2$ that is plotted in Fig. 1b. Hence, the magnetization is pointed in the XZ plane. The texture in Fig. 1b is found via matching solutions of positive and negative $q^{'}$ on the lines $\varphi = 0$ and $\varphi = \pi$.

The texture of circumferentially magnetized domains in Figs. 1c corresponds to (7) with $|q^{''}|R = 1$, $s^2 \approx 1$, $\phi = \pi/2$ (plotted in Fig. 1d). Besides the vicinities of the wire ends, the domains of Fig. 2a are similar to those of Fig. 2b. The plot of Fig 2b has been obtained similar to that of Fig. 1d while taking $|q^{''}|R = 4$. The centers of vortices and antivortices which are contained in the structure of the DWs lie on the lines $\varphi = n\pi/4$, where $n = 0, 1, \ldots, 7$. From Fig. 2b the relevant DWs are seen to be of the cross-tie type similar to the DWs of Fig. 2a. Note that a denser bamboo-like domain structure has been established within simulations of a similar to ours nanotube of a ferromagnet with considerably larger magnetostatic exchange length than that of Co [30]. We mention that microscopic mechanism responsible for appearance of the hard-axis anisotropy (positive axial stress), thus, for creation of the bamboo-like textures in glass-coated wires of the materials with negative magnetostriction is not completely clear to date [18], however, it is known to be activated during the cooling process. In the thin-wall tubes (rolled-up nanomembranes) it seems to be especially efficient because of smaller solidification stresses than in the wires. A general model of a similar DW to that of Fig. 1c while including effects of finite thickness of the tube wall ([31]) has been formulated in [32]. A cross-tie DW similar to those in Fig. 2a and Fig. 2b has been simulated in [33].

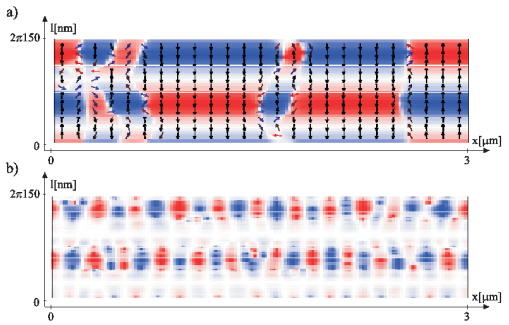

Figure 4: The textures established in the Co tube of 300nm diameter, 3μm length, 20nm wall thickness (a) and 5nm wall thickness (b) with the random initial orientations of the magnetization. The material parameters, the reference frame and meaning of colors are the same as in Figs. 1-2. In b), the arrows are omitted for better visibility.

In Fig. 3a, the relaxed magnetization of the tube of 450nm diameter, 20nm wall thickness and 3μm length, and initially magnetized perpendicular to the long axis ($\mathbf{m}(t=0) = [0, M_s, 0]$) is visualized. Without detailed estimation of the stress, we include the arbitrary value of the constant of the solidification-stress induced anisotropy $K_a^{(cool)} = -0.63\cdot 10^5 \mathrm{J/m^3}$ that is reduced compared to that applied in the simulations of the tubes of 300nm diameter. The reduction in the stress due to the reduction of the tube-surface curvature is expected and it results in a decrease of the effective anisotropy constant. The texture is found to contain vortices and antivortices whose centers are magnetized along the axis of the initial magnetization of the tube.

The texture from Fig. 3a can be quite well described locally with the static solution (8) to the LLG equation. In the sections of the tube; $0 < \varphi < \pi/2$ and $\pi < \varphi < 3\pi/2$ in Fig. 3b, (these sections correspond to sections 2 and 4 in Fig. 3a), $w=0$ and $k^{''}=0$, thus, $q^{'2} = (\beta_1 - \beta_3)/J$. Since $\beta_1 > \beta_3$, the magnetostatic contribution to the anisotropy constant oversizes the magnetostrictive contribution leading to the easy-axis. In the remaining (vortex-containing) sections of the tube (which correspond to sections 1 and 3 in Fig. 3), there are no well-defined domains, thus, there is no easy direction of the magnetization in the plane of the tube surface. There, the magnetostatic (shape) contribution to the the anisotropy constant has to be compensated by the stress contribution, thus, $q^{'2} \approx \tilde{k}^{''2}$. In Fig. 3b, in each of four $h\pi/2 < \varphi < (h+1)\pi/2$ sections, $(h = 0, 1, 2, 3)$; $q^{'} 2\pi R/s = 2K(s)$.

Finally, we have simulated the relaxation from a disordered initial state (a random magnetization orientation). In the system of Figs. 1-2, (the Co tube of 300nm diameter, 3m length, and 20nm wall thickness), the resulting state is formed of several circumferentially-magnetized domains which are of different (irregular) lengths (Fig. 4a). However, for the 5nm tube-wall thickness, the domains of

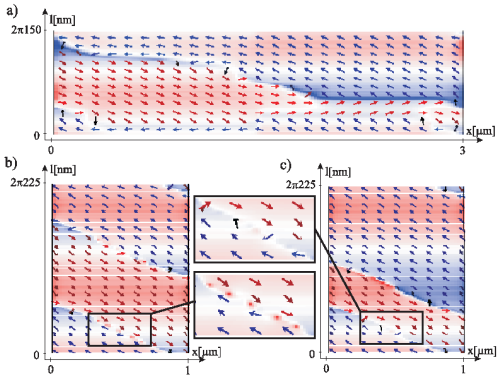

Figure 5: The stable texture established in the Py tube: a) of 300nm diameter, 3μm length, and 20nm wall thickness, and helical anisotropy constant $K_h^{(solid)} = -0.3 \cdot 10^5 \mathrm{J/m}^3$, with the initial magnetization $[0, M_s, 0]$; b) and c) of 450nm diameter, 1μm length, and 20nm wall thickness, $K_h^{(solid)} = -1.0 \cdot 10^5 \mathrm{J/m}^3$, with the initial magnetization $[0, M_s, 0]$ and $[M_s/\sqrt{2}, M_s/\sqrt{2}, 0]$ respectively. Meaning of colors is the same as in Figs. 1-2. In the inset of b), a chain of vortex (antivortex) cores of the same polarity is seen inside the DW. In the inset of c), a single isolated defect (a vortex without any clear polarity) is seen in the DW.

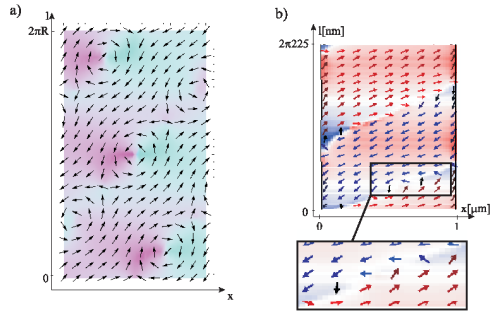

Figure 6: Plot of a spatially-periodic solution to the XY model on the tube surface (a). The stable texture (b) established in the Co tube of 450nm diameter, 1μm length, and 20nm wall thickness, and helical anisotropy constant $K_h^{(solid)} = -1.0 \cdot 10^5 \mathrm{J/m}^3$, with the initial magnetization $[0, M_s, 0]$. Meaning of colors is the same as in Figs. 1-2.

circumferential magnetization are very short while the texture becomes almost periodic (Fig. 4b). That state of a tube with an ultra-thin wall resembles a periodic texture found in Ref. [30] within 2D micromagnetic simulations.

3.2. Tubes with solidification-dominated stress

The tubes of Py have been simulated with the following material constants: $M_s = 0.86 \cdot 10^6 \mathrm{A/m}$, $A_{ex} = 1.3 \cdot 10^{-11} \mathrm{J/m}$. In the regime of the solidification-dominated stress, visible effects are expected to result from specific orientations of the easy direction in the tube wall. This anisotropy is induced by the material deposition at the stage of the production of the magnetic layer. We simulate the Py tube with a resulting helical anisotropy whose axis is deviated by $\pi/4$ angle from the long axis of the stripe in the tube wall (directed along $[\sqrt{y^2+z^2}, -z, y]$ vector). If this anisotropy is sufficiently strong, it drives the spiral orientation of the magnetization inside the domains. We consider a constant the helical anisotropy in the range $K_h^{(solid)} \sim (-1) \cdot 10^4 \div (-1) \cdot 10^5 \mathrm{J/m}^3$. Notice that in-the-plane anisotropy of the constant (absolute value) close to $10^4 \mathrm{J/m}^3$ has been reported for flat and rolled-up nanomembranes of Py [9], and for Co film [16].

In Fig. 5a, the resulting ordering of Py tube of 300nm diameter, 20nm wall thickness, 3μm length and of $K_h^{(solid)} = -0.3 \cdot 10^5 \mathrm{J/m}^3$ is visualized. In this quite elongated and of weak anisotropy tube, the competition between the shape and structural anisotropy creates a 'frustration' of the magnetic moments. They orient along the tube axis at some parts of the tube while, at other parts, they tend to point onto the spiral line. In consequence, there are no well separated (by DWs) ferromagnetic domains in the texture of Fig. 5a.

The next two visualizations (Figs. 5b, 5c) represent the static ordering of the Py tube of 450nm diameter, 20nm wall thickness, 1μm length and of $K_h^{(solid)} = -1.0 \cdot 10^5 \mathrm{J/m}^3$. Its longitudinal (shape) anisotropy is reduced compared to the structure of Fig. 6a due to the small length of the system and the ordering is dominated by the material anisotropy. The well defined domains of spiral ordering are shown to be separated by DWs which are parallel to the domain magnetization. Similar to the simulations of the tubes with cooling-dominated stress, the final state of the magnetization relaxation is dependent on the initial state. For instance, in Figs. 5b and 5c, the stable textures obtained with the homogeneous initial states $\mathbf{m}(t=0) = [0, M_s, 0]$ and $\mathbf{m}(t=0) = [M_s/\sqrt{2}, M_s/\sqrt{2}, 0]$, respectively, are presented. The stabilized textures differ not only in the position of the DWs, while also in the DW structure.

The ordering in Fig. 5b coincides with the analytically predicted DW textures for the XY model. The relevant DW-containing texture described with (10) for $|\eta| = \pi/4$ is plotted in Fig 6a. Such a DW contains alternating vortices and antivortices whose polarity is not determined by the model. In the inset of Fig. 5b, one sees all singularities of the DW to can be of the same polarity. This is not obtainable from direct cross-tie-DW solutions to the LLG equation of the one-axis ferromagnet in 2D whose vortex and antivortex polarities are opposite [20, 21]. In contrast, the DWs in Fig. 5c are not of the cross-tie structure.

In Fig. 6b, the result of the simulation of the cobalt tube of the same sizes as the tube in Fig. 5b with similar initial condition $\mathbf{m}(t=0) = [0, M_s, 0]$ is presented. In the Co tube, very different (Neel-like) DWs from (cross-tie) DWs of the Py tube are found because of bigger exchange length of the helical anisotropy l_K for Co ($l_K = 18.2$nm) than for Py ($l_K = 11.4$nm). This shows the inapplicability

of the XY model to the Co tube contrary to the Py tube. Noticeably, the applicability of the XY model is dependent on the initial conditions as well, which follows from the difference in the DW structures in Fig. 5b and Fig. 5c.

Due to finite length of the tube, the DWs in Figs. 5c,6b are not perfect Neel structures while contain isolated vortices which are not predicted by our analytical description of the infinite tubes. We note that the polarities of large-core vortices (antivortices) present in the textures of Figs. 3,5c,6b are not determined by the simulations because of internal domain structure of the vortex and antivortex [34].

Studying the relaxation of tubes of different wall thicknesses from the state of randomly-distributed orientations of the magnetization, for a wide range of the material parameters and tube sizes, with $\pi/4$ angle of the easy-axis deviation from the tube long axis, we find the resulting texture to be a helical single-domain state. In particular, for the systems of Fig. 5 and Fig. 6. The magnetization is oriented along the easy direction in the tube surface. However, the initial stage of the relaxation process in thin-wall tubes is found to be the formation of a quasi-periodic state that contains long oppositely-magnetized helical domains. Formed with the random initial condition, those striped domains appear not to be stable and slowly collapse into a mono-domain (helically-magnetized) state. We mention that the observation of striped helical domains in the rolled-up nanomembranes has been reported however [9]. Perhaps, upon being created, they are stabilized by tube imperfections; structural defects or a jump on the tube surface that corresponds the edge of the rolled-up sheet of a ferromagnetic material.

4. Conclusions

A series of analytical static solutions to LLG equation for an effective model of the ferromagnetic thin-wall tube has been found analyzing different parameter regimes. The applicability of the solutions of our model (that is based on the substitution of the magnetostatic field in the tube with a contribution to an effective anisotropy field) has been verified using the micromagnetic simulations. Including one of two (axial or helical) types of the effective anisotropy, the model appeared to be capable to describe basic features of the ordering in ferromagnetic thin-wall tubes.

It has been established that main characteristics of the magnetic textures (the number, size, and shape of the domains) are governed by the stress-induced anisotropy. Since the stress in the tube is sensitive to details of the tube fabrication, the ordering is not universal result of the material and size parameters. Moreover, a strong dependence of the ordering on initial state of the structure formation process is noticed. In spite of this, there is a quite limited basis of possible magnetization textures of the tube and factors influencing their choice are identified.

Details of textures (the structure of the DWs) are dependent on the ratio of the magnetostatic exchange length to the exchange length of the stress-driven anisotropy. This makes a problem for efficiently simulating tubes (rolled-up nanomembranes) of the sub-μm- and μm-radii due to large computational resources needed when including the magnetostatic (dipole) interactions. To date, in order to avoid this problem, any approach to the micromagnetic simulations of such systems of a large-number of the magnetic moments is based on oversizing the length of the grid discretization over the magnetostatic exchange length [35, 36]. This can result in overseeing some texture details. Our analytical model enables inclusion of them into the tube description.

Finally, we mention that we have not considered nano-nor microtubes (rolled-up nanomembranes) with perpendicular magnetic anisotropy. In those hard-magnetic systems a dense structure of radially magnetized domains is spontaneously created, e.g. in rolled-up Co/Pt and Co/Pd layers [37, 38]. It is similar to that observed in the outer shell of the amorphous or polycrystalline glass-coated microwires with positive magnetostriction constant as a result of the competition between the stress-driven radial easy-axis anisotropy and the surface (magnetostatically-induced) radial anisotropy of the hard-axis type [10, 39]. Since the layers with perpendicular magnetic anisotropy are ultra-thin, 3D micromagnetic simulations of those tubes are challenging, (they require the grid discretization with very small cells), even for nanometer-sized radii of the tubes. On the other hand, unlike in the microwires with positive magnetostriction, the surfaces of the DWs in such tubes are extremely small, thus, pinning of them to structure defects is very strong. This makes the magnetic ordering irregular (spatially aperiodic) while dominated by structural properties.

References

[1] N. A. Buznikov, et al., Giant magnetoimpedance in composite wires with insulator layer between non-magnetic core and soft magnetic shell, J. Magn. Magn. Mat. 300 (2006) e63.

[2] J. Torrejon, G. Infante, G. Badini-Confalonieri, K. R. Pirota, M. Vazquez, Electroplated Bimagnetic Microwires: From Processing to Magnetic Properties and Sensor Devices, JOM, 65 (2013) 890.

[3] M. Sedlar, V. Matejec, I. Paulicka, Optical fiber magnetic field sensors using ceramic magnetostrictive jackets, Sensors and Actuators, 84 (2000) 297.

[4] I. Monch, et al., Rolled-Up Magnetic Sensor: Nanomembrane Architecture for In- Flow Detection of Magnetic Objects, ACS Nano, 5 (2011) 7436.

[5] Y. C. Sui, R. Skomski, K. D. Sorge, D. J. Sellmyer, Nanotube magnetism, Appl. Phys. Lett. 84 (2004) 1525.

[6] K. Nielsch, F. J. Castano, C. A. Ross, R. Krishnan, Magnetic properties of template-synthesized cobalt/polymer composite nanotubes, J. Appl. Phys. 98 (2005) 034318.

[7] Y. Ye, B. Geng, Magnetic Nanotubes: Synthesis, Properties, and Applications, Crit. Rev. Sol. State Mater. Sci. 37 (2012) 75.

[8] F. Borza, T.-A. Ovari, S. Corodeanu, G. Stoian, H. Chiriac, Magnetic Properties of CoFeSiB/(Co, CoPtRh) Multilayer Microwires, IEEE Trans. Magn. 51 (2015) 2005204.

[9] R. Streubel, et at., Magnetic Microstructure of Rolled-Up

Single-Layer Ferromagnetic Nanomembranes, Adv. Mater. 26 (2014) 316.
[10] H. Chiriac, T. A. Ovari, Amorphous glass-covered magnetic wires: preparation, properties, applications, Prog. Mater. Sci. 40 (1996) 333.
[11] A. Antonov, A. Dykhne, A. Lagarkov, N. Usov, Structure of 90^o domain wall in Co-based amorphous wire, Physica A 241 (1997) 425.
[12] J. Torrejon A. Thiaville, A. L. Adenot-Engelvin, M. Vazquez, O. Acher, Cylindrical magnetization model for glass-coated microwires with circular anisotropy: Statics, J Magn. Magn. Mat. 323 (2011) 283.
[13] T.-A. Ovari, S. Corodeanu, H. Chiriac, Near-Surface Magnetic Structure and GMI Response in Amorphous Microwires, IEEE Trans. Magn. 45 (2009) 4282.
[14] Y. Zhao, H. Hao, Y. Zhang, Preparation and giant magneto-impedance behavior of Co-based amorphous wires, Intermetallics 42 (2013) 62.
[15] G. V. Kurlyandskaya, N. G. Bebenin, V. O. Vaskovsky, Giant magnetic impedance of wires with a thin magnetic coating, Phys. Metals and Metallography 111 (2011) 133.
[16] S. van Dijken, G. Di Santo, B. Poelsema, Influence of the deposition angle on the magnetic anisotropy in thin Co films on Cu(001), Phys. Rev. B 63 (2001) 104431.
[17] S. Cherifi, et al., Tuning the domain wall orientation in the thin magnetic strips using induced anisotropy, Appl. Phys. Lett. 91 (2007) 095202.
[18] N. A. Usov, O. N. Serebryakova, The pecularities of magnetization reversal process in magnetic nanotube with helical anisotropy, J. Appl. Phys. 116 (2014) 133902.
[19] M. M. Bogdan, A. S. Kovalev, Exact multisoliton solution of one-dimensional Landau-Lifshitz equations for an anisotropic ferromagnet, JETP Lett. 31 (1980) 424.
[20] K. L. Metlov, Simple analytical description for the cross-tie domain wall structure, Appl. Phys. Lett. 79 (2001) 2609;
K. L. Metlov, Cross-tie domain wall ground state in thin films, J. Low Temp. Phys. 139 (2005) 207.
[21] A. Janutka, Externally driven transformations of vortex textures in flat submicrometer magnets, Phys. Rev. B 85 (2012) 184421.
[22] A. Janutka, Short-range interactions of domain walls in ferromagnetic nanostripes, IEEE Magn. Lett. 4 (2013) 4000304.
[23] O. Tchernyshyov, G.-W. Chern, Fractional vortices and composite domain walls in flat nanomagnets, Phys. Rev. Lett. 95 (2005) 197204.
[24] S. Middelhoek, Domain Walls in Thin NiFe Films, J. Appl. Phys. 34 (1963) 1054.
[25] C. Muller, et al., Tuning magnetic properties by roll-up of Au/Co/Au films into microtubes, Appl. Phys. Lett. 94 (2009) 102510.
[26] R. Streubel, et al., Rolled-up Permalloy nanomembranes with multiple windings, SPIN 3 (2013) 1340001.
[27] S. Min, et al., Novel approach to control diameter of self-rolled magnetic microtubes by anodizing Ti layer, IEEE Magn. Lett. 3 (2012) 400304.
[28] D. Ruffer, et al., Magnetic states of an individual Ni nanotube probed by anisotropic magnetoresistance, Nanoscale 4 (2012) 4989.
[29] math.nist.gov/oommf/
[30] N. A. Usov, A. Zhukov, J. Gonzalez, Domain structure of magnetic nanotube with transverse anisotropy, Phys. Stat. Sol. A 208 (2011) 535.
[31] A. P. Chen, J. Gonzalez, K. Y. Guslienko, Domain walls confined in magnetic nanotubes with uniaxial anisotropy, J. Magn. Magn. Mat. 324 (2012) 3912.
[32] A. P. Chen, J. Gonzalez, K. Y. Guslienko, Axially symmetric domain walls confined in ferromagnetic nanotubes, Mater. Res. Express 2 (2015) 126103.
[33] I. Betancourt, G. Hrkac, T. Schref, Micromagnetic simulation of domain wall dynamics in Permalloy nanotubes at high frequencies, J. Appl. Phys. 104 (2008) 023915.
[34] H. Youk, G.-W. Chern, K. Merit, B. Oppenheimer, O. Tchernyshyov, Composite domain walls in flat nanomagnets: The magnetostatic limit, J. Appl. Phys. 99 (2006) 08B101.
[35] L. Stoleriu, C. Pinzaru, A. Stancu, Micromagnetic analysis of switching and domain structure in amorphous metallic nanowires, Appl. Phys. Lett. 100 (2012) 122404.
[36] P. Gawroński, A Chizhik, K. Kułakowski, Simulated hysteresis loop of a bent Fe-rich glass-covered wire, arXiv: 1508.01692.
[37] J. Zarpellon, et al., Magnetic domains in rolled-up nanomembranes of Co/Pt multilayers with perpendicular magnetic anisotropy, RCS Adv. 4 (2014) 8410.
[38] R. Streubel, F. Kronast, P. Fischer, D. Parkinson, O. G. Schmidt, D. Makarov, Retrieving spin textures on curved magnetic thin films with full-field soft X-ray microscopies, Nature Comm. 6 (2015) 7612.
[39] Yu. Kabanov, A. Zhukov, V. Zhukova, J. Gonzalez, Magnetic domain structure of wires studied by using the magneto-optical indicator film method, Appl. Phys. Lett. 87 (2005) 142507